Remote Sensing Applications: Society and Environment 24 (2021) 100617

Contents lists available at ScienceDirect

Remote Sensing Applications: Society and Environment

journal homepage: www.elsevier.com/locate/rsase

Reappraisal of DEMs, Radar and optical datasets in lineaments extraction with emphasis on the spatial context

Ali Shebl [a,b,*], Árpád Csámer [a]

[a] Department of Mineralogy and Geology, University of Debrecen, Egyetem tér 1, 4032, Debrecen, Hungary
[b] Department of Geology, Tanta University, Tanta, 31527, Egypt

ARTICLE INFO

Keywords:
Lineament extraction
ALOS PALSAR DEM
Sentinel 1
DEMs
Geological structures
Landsat OLI
ASTER
Sentinel 2A

ABSTRACT

Lineaments mapping is an authentic issue for deciphering the tectonic setting, geological history, mineral prospecting, and other several applications. Consequently, the study objective is to examine various remote sensing datasets at wide various spatial resolutions (10, 12.5, 15, 20, 30 m), to recommend the best in lineaments elicitation, for usage in the geological scientific community. Toward this aim, nine various remote sensing datasets including optical sensors (Landsat OLI, ASTER, Earth Observing-1 Advanced Land Imager, Sentinel 2A), radar data (Sentinel 1), and digital elevation models (ALOS PALSAR, SRTM, NASA, ASTER V3), are tackled. In this scope, we created an entirely automatic lineament derivation environment through the integration of edge detection and line-linking algorithms. Results show that the used optical sensors are less efficient than DEMs having the same spatial resolution. Sentinel 1 radar data is more competent than optical data sources. ALOS PALSAR DEM (12.5m) is more eligible than any other utilized data type even sentinel 1 data (10 m). Wholly, DEMs built from radar data (e.g., PALSAR DEM) proved their leverage in lineament extraction to a limit that can deviate from the well-known relationship between the number of extracted lineaments and pixel size.

1. Introduction

Lineaments are considered essential features for most surficial studies and represent the key for solving various issues in several disciplines (Pirasteh et al., 2013). Geologically, linear tectonic features which may be faults, dykes, and shear zones are considered yardsticks in several surface and subsurface studies, such as, ore deposits and mineral prospecting (Abd El-Wahed et al., 2021; Manuel et al., 2017; Pour et al., 2016; Pour and Hashim, 2015a; Shebl et al., 2021), hydrogeology (Adiri et al., 2017; Akinluyi et al., 2018; Bhuiyan, 2015; Dasho et al., 2017; Hashim et al., 2013; Koike and Ichikawa, 2006; Qari, 2011; Takorabt et al., 2018), petroleum exploration (Marghany and Hashim, 2010), engineering constructions (Adhab and Hassan, 2014; Rahnama and Gloaguen, 2014; Sukumar et al., 2014), landslides (Alizadeh et al., 2018; Ashournejad et al., 2019), placement of conceivable geothermal reservoirs (Saepuloh et al., 2018), and groundwater exploration (Bruning et al., 2011; Ibrahim and Mutua, 2014; Magaia et al., 2018). The identification of lineaments in an automatic way is more efficient and much faster than the manual (visual) process, which is influenced by subjective parameters like quality analysis and experience (Muhammad and Awdal, 2012). Recently, the availability of a various and wide range of remote sensing datasets and their potency to supply steady obvious data across large areas compared to ground-based assessments, offer an easier approach compared to the manual methods for lineaments extraction. Consequently, the latest two decades have witnessed considerable advances in scientific research toward assessing linear features, using several techniques and in various applications (Hashim et al., 2013; Meshkani et al., 2013; Nath et al, 2017, 2019; Pour et al., 2016; Pour and Hashim, 2014, 2015b; Singh and Garg, 2013). The automatic methods have resulted in a more efficient lineament extraction process (Masoud and Koike, 2006, 2011; Tripathi et al., 2000). A lineament extraction process comprises two main steps, namely edge detection, and line-linking or line extraction, utilizing digital data like satellite images, determining algorithms, and certain software like the frequently used LINE module of PCI Geomatica.

The main objective of this study is to compare and examine the potentialities of the most currently used data types of the three main categories; optical, radar, and DEMs considering various spatial resolutions (10, 12.5, 15, 20, 30 m) to build a suitable recommendation to be famed for automatic lineaments extraction process. To achieve this aim, an enormous amount of data was obtained, preprocessed, and processed, in a GIS environment. More than 100 lineament maps, from different

* Corresponding author. Department of Mineralogy and Geology, University of Debrecen, Egyetem tér 1, 4032, Debrecen, Hungary.
E-mail address: ali.shebl@science.tanta.edu.eg (A. Shebl).

https://doi.org/10.1016/j.rsase.2021.100617
Received 19 May 2021; Received in revised form 19 August 2021; Accepted 20 August 2021
Available online 22 August 2021

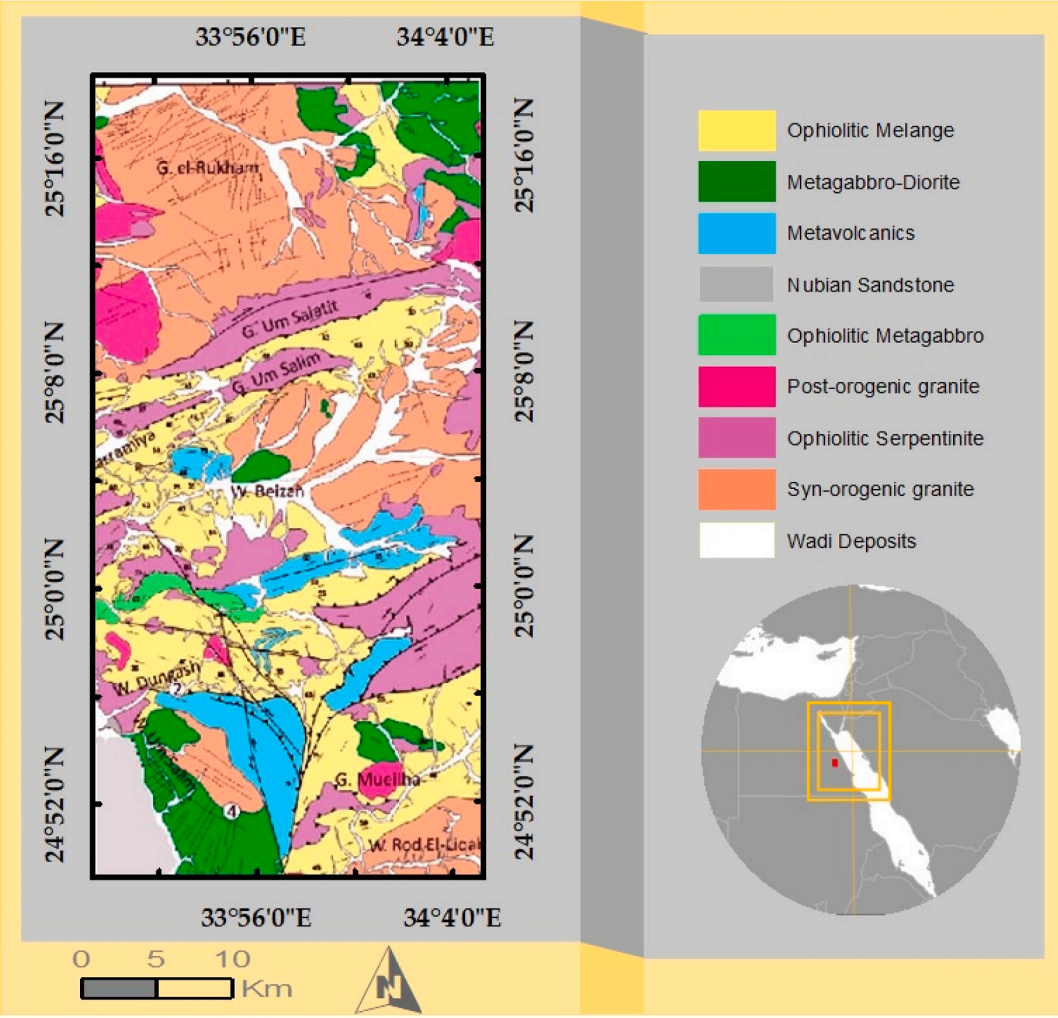

Fig. 1. Geological map of the study area showing its lithological units, after (Zoheir et al., 2019a).

sources, were established and compared to be efficiently judged, under unifying most of the parameters and making the only variable is the data type. The data used in this study include multispectral data (Landsat 8 OLI, ASTER, EO1 ALI, Sentinel 2A), radar data (Sentinel 1), and DEMS (ALOS PALSAR, SRTM, NASA, ASTER V3).

2. Data and methods

2.1. Study area

Um Salatit – Mueilha area is located at the extreme southern part of the Central Eastern Desert (CED), Egypt. It extends between latitudes 24° 49" to 25° 18" N and longitudes 33° 50" to 34° 05" E covering an area of about 1400 km^2. The investigated area was selected for this

Table 1
Characteristics of the utilized optical datasets.

Landsat 8			ASTER			Sentinel 2			EO1 ALI		
B.n	C.W. (μm)	S.R (m)	B.n	C.W. (μm)	S.R (m)	B.n	C.W. (μm)	S.R (m)	B.n	C.W. (μm)	S.R (m)
1	0.442	30	1	0.560	15	1	0.443	60	Pan.	0.585	10
2	0.483	30	2	0.660	15	2	0.490	10	1	0.443	30
3	0.561	30	3N	0.820	15	3	0.560	10	2	0.482	30
4	0.654	30	3B	0.820	15	4	0.665	10	3	0.565	30
5	0.864	30	4	1.650	30	5	0.704	20	4	0.660	30
6	1.609	30	5	2.165	30	6	0.740	20	5	0.790	30
7	2.203	30	6	2.205	30	7	0.782	20	6	0.867	30
8	0.598	15	7	2.260	30	8	0.842	10	7	1.250	30
9	1.373	30	8	2.330	30	8a	0.865	20	8	1.650	30
10	10.90	100	9	2.395	30	9	0.945	60	9	2.215	30
11	12.00	100				10	1.375	60			
						11	1.610	20			
						12	2.190	20			

Band number (B.n), Central wavelength (C.W), Spatial Resolution (S.R) and Pan for panchromatic.

work, as it is famous for old mining activities, dykes, faults, hydrothermal alteration zones, which manifest the role of lineaments in controlling mineralization. Furthermore, it has a recently published geological map, which is useful in comparing and verifying the results. Geologically, the considered area is covered mainly by a widely distributed stretch of Neoproterozoic ophiolitic mélange constituted mainly of allochthonous ophiolitic fragments blended in a sheared matrix, as well as, other different mappable units (Zoheir et al., 2019a). Ophiolitic mélange is considered the most extensive unit of the area. The other mappable units include metavolcanics, metagabbro-diorites, and granitic rocks as shown in Fig. 1.

2.2. Data characteristics and preprocessing

A Landsat-8 (L8) scene, with an ID of LC81740432019298LGN00, and acquired on October 25, 2019 with a path 147 and row 43, covers the whole study area. Also, the investigated area is entirely covered by Advanced Spaceborne Thermal Emission and Reflection Radiometer (ASTER) scene named AST_L1A_00303062007083043, and acquired on March 6, 2007. Earth Observing-1 Advanced Land Imager (ALI) data used in this study (EO1A1740422003070110PZ) was acquired in 2003 and imaged by ALI sensor. L8, ASTER, and ALI are attained through the U.S. Geological Survey Earth Resources Observation and Science Center (EROS) (https://earthexplorer.usgs.gov/) and their characteristics are described in Table 1. Sentinel 2 (S2) data Utilized in the current study is obtained through the European Space Agency (ESA). A cloud-free, S2A MSI scene (S2A_MSIL1C_20200505T081611_N0209_R121_T36RWN_20200505T095132) was acquired on May 5, 2020, and its characteristics are summarized in Table 1. The utilized multispectral optical data of Landsat-8 level 1T, ASTER (AST_L1A), and ALI are geometrically corrected according to UTM, WGS 84 zone 36 N. Consequently, running Fast Line-of-Sight Atmospheric Analysis of Spectral Hypercubes (FLAASH) atmospheric correction, resizing the data to the borders of the study area. Sentinel-2 Dataset bands were geo-referenced to the zone 36 North UTM projection using the WGS-84 datum then, radiometrically-corrected using sen2cor processor in Sentinel Application Platform (SNAP). Time of acquisition is the main controller of the shadows within optical images. Thus, Unifying the time of imaging was desired during the data selection phase to remove any preferability among the datasets as differences in the time result in different shades which directly affect the detected lineaments. Time of scene acquisition was 07:59:31, 08:03:44, 08:13:29, and 8:16:11 for EO1 ALI, ASTER, Landsat OLI, and Sentinel 2. We also tried to preserve sun angles within the same range as much as we can (e.g., 50.38, 52.7, 48.94 for EO1 ALI, ASTER, Landsat OLI respectively). On the other hand, the current research data considers timings of seasonal events, which may affect the quality of optical images and the evaluation feasibility by selecting all the optical data in months of steady climatic conditions. After revising the timings of major flash flood events within the study area and its environs, it was found that most of these events are evident between November and February. Consequently, All the optical scenes are acquired beyond this time range.

Shuttle Radar Topography Mission (SRTM) was flown aboard the space shuttle Endeavour on 11–22 February 2000. For this study, SRTM DEM was obtained from the USGS Earth Explorer web-based data (https://earthexplorer.usgs.gov) to extract lineaments within the study area. NASADEM product (30m) is a state-of-the-art global digital elevation model (DEM) derived from a combination of SRTM processing improvements, elevation control, void-filling, and merging with data unavailable at the time of the original SRTM production. NASA DEM is distributed in 1° by 1° tile and consist of all land between 60° N and 56° S latitudes. For this study, NASA DEM was obtained from the USGS web-based data (https://lpdaac.usgs.gov/). Advanced Spaceborne Thermal Emission and Reflection Radiometer–Global Digital Elevation Model (ASTER GDEM) has 1 arc-second (30 m) spatial resolution, and this project is done by the Ministry of Trade, Economy and Industry (METI) of Japan and the United States National Aeronautics and Space Administration (NASA) to provide high-resolution DEM to the public. In this study, four scenes (ASTGTMV003_N24E033, ASTGTMV003_N24E034, ASTGTMV003_N25E033, and ASTGTMV003_N25E034) were obtained, mosaicked to one raster, and resized to the area outline. The Advanced Land Observing Satellite (ALOS) was launched on January 24, 2005. ALOS has three remote-sensing instruments: Panchromatic Remote-sensing Instrument for Stereo Mapping (PRISM) for digital elevation mapping, the Advanced Visible and Near Infrared Radiometer type 2 (AVNIR-2) for precise land coverage observation, and the Phased Array L-type band Synthetic Aperture Radar (PALSAR) for day-and-night and all-weather land observation. From Alaska Satellite Facility (https://asf.alaska.edu/), ALOS-PALSAR FBS (Fine Beam Single polarization mode, HH) RT1 (Radiometric Terrain Corrected with Pixel spacing is 12.5 m) DEM is used in this work to extract the linear features of the study area. PALSAR sensor is an active microwave sensor (help to avoid weather barrier conditions and day or night effect), L-band (1.27 GHz) synthetic aperture radar aid at achieving high-resolution DEM products. All DEMS are geometrically corrected and prepared to obtain 16 shaded reliefs with different azimuths (0°, 45°, 90°, 135°, 180°, 225°, 270°, and 315°), and altitudes (at 30° and 45°) using spatial analyst tools in ArcMap.

Sentinel-1 is the premier satellite of the Copernicus Programme satellite constellation conducted by ESA. The first satellite, Sentinel-1A, launched on April 3, 2014, and Sentinel-1B on April 25, 2016. They carry a C-band synthetic-aperture radar (SAR) instrument, which provides a collection of data in all-weather, day or night. In Sentinel 1, scattered energy recorded as radar data is considered one of the most powerful techniques in extracting lineaments. Radar data can be transformed into bands depending on the signals transmitted to, and received back from, land surfaces (e.g., Horizontal send and Horizontal receive: HH, and Horizontal send and Vertical receive: HV), and the intensity, as well as polarization, can provide insights into the scattering mechanisms and, hence, the physical structure of scattering elements (e.g., lineaments). Furthermore, techniques, such as interferometric synthetic aperture radar (InSAR), use differential phases of reflected signals to detect land surface changes and can be used to map various land properties (Engdahl and Hyyppa, 2003; Hong and Wdowinski, 2014). Higher look angles mostly manifest topographic attributes in flat terrain but exaggerate shadowing in areas of high reliefs. Contrarily, smaller incidence angels severely distort higher reliefs (Richards and others, 2009). Thus, a mid-angle (33°), standard Dual Polarization (SDV), Ground Range Multi-Look Detected (GRD), High Resolution (HR) product, with approximately square pixel spacing product, was found to be suitable with the varied topography and different lineaments representations within the study area (e.g., controlled drainage lines, gentle and steep tectonic fractures, dykes with various orientations and dips, rock boundaries with varied attitudes and elevations). Moreover, these products almost deliver images with reduced speckle. Sentinel-1A of Interferometric Wide (IW) mode and pixel-spacing 10 m × 10m, obtained from ESA to fulfill the aim of this study. The Granule ID: S1A_IW_GRDH_1SDV_20200926T154707_20200926T154736_034532_0404DC_2A0B, acquired on September 26, 2020. Sentinel-1 data was preprocessed by applying several steps including the precise orbit of acquisition, removing thermal and image border noise, radiometric calibration, and range-doppler and terrain correction using SNAP toolbox.

2.3. Processing (Lineament extraction)

2.3.1. Automatic extraction

The major preference of automatic technique is its vantage of lineaments detection that could not be perceived and observed by naked eyes (Adhab and Hassan, 2014) as well as, saving time and effort compared to visual extraction. Lineament detection utilizing computer algorithms relies basically on two concepts, the first is edge detection

Table 2
The assigned values and tasks for the LINE module parameters.

		Mission	Value
Edge detection	**RADI**	To detect contours efficiently	10
	GTHR	To determine the pixels value considered as edges	50
Curve extraction	**LTHR**	To omit shorter curves having number of pixels lower than LTHR value	30
	FTHR	To generate polylines fitting FTHR value	3
	ATHR	Linking polylines with end point angle coinciding with ATHR	15
	DTHR	Joining polylines whose endpoints respect DTHR value	20

and the second is line extraction. The most widely used, LINE module of the PCI Geomatica software is employed for this study. To accomplish this task, several parameters are required to determine the edges and, curves taken into consideration to ensure a reasonable level of lineament extraction. These parameters are RADI (filter radius), GTHR (Edge Gradient Threshold), LTHR (Curve Length Threshold), FTHR (Line Fitting Threshold), ATHR (Angular Difference Threshold), and DTHR (Linking Distance Threshold). Table 2, defines the importance of each parameter in the process of extraction. Depending on the previous studies, literature, default values, and experimenting with more than 20 permutations of the previously mentioned parameters over different data types, the applied values in this study are determined and tabulated in Table 2. These assigned parameters are kept constant in all the stages and during all phases of automatic extraction of lines to ensure equitable comparison of all data. For RADI, this study implemented Canny filter due to its ability to detect contours as proved in previous studies (Corgne et al., 2010; Marghany and Hashim, 2010). GTHR uses the RADI product image to obtain a binary image depending on the discrimination of edge values from the remaining background using a certain value. The latter binary product is converted to curves depending on LTHR value, only curves with a higher value than LTHR are considered and extracted as lines. The lines coinciding with the FTHR value are, in turn, converted to polylines. The last step is polyline transformation to lineaments, this is only evident depending on the angular value (ATHR) and distance (DTHR) between endpoints of a line. The input data for the automatic extraction process are more than 100 images from different sources and by different spatial resolutions, including 41 images from optical data, 64 images from DEMs, and 2 images from Sentinel 1 radar data. The PCI line module is executed over all these inputs separately and by utilizing the same previously mentioned parameters to get more than 100 lineament maps.

2.3.2. *Manual extraction*

This visual method involves three main steps: image processing, visual interpretation, and manual digitization of the lineaments (Ibrahim and Mutua, 2014). To ensure an efficient manual delineation of lineaments, image enhancement techniques (e.g., optimum index factor) are calculated for the data, to enhance all types of lineaments e.g., geological structures (faults, joints, dykes), geomorphological (cliffs, terraces, topographic alignments, and controlled stream segments), tonal contrast (various rock compositions), and even anthropogenic activities and effects (roads). Also, the PCA data transformation technique was

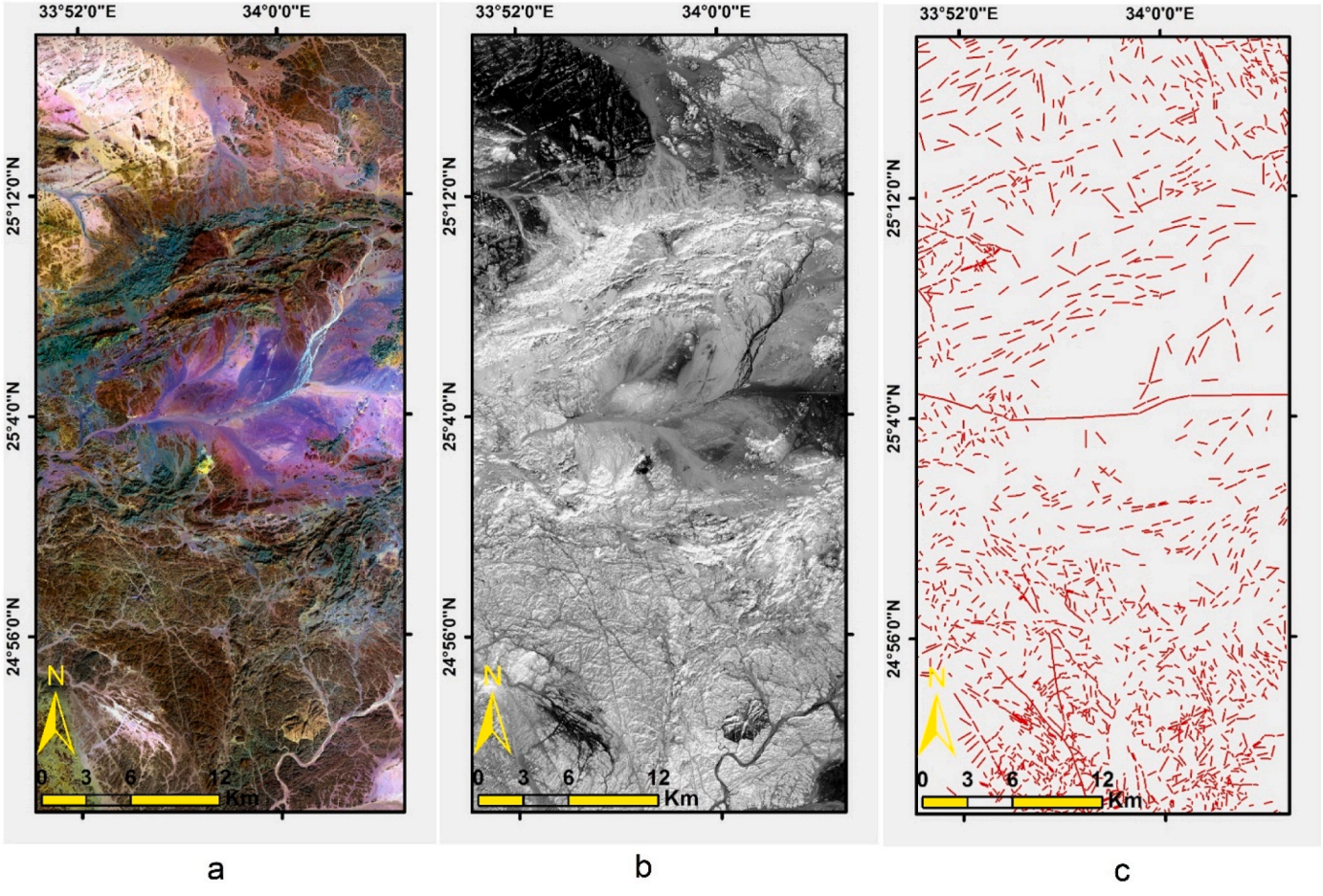

Fig. 2. Manual digitization of lineaments from 15m resolution data: (a) RGB 752 pan-sharpened HSV L8 and, (b) PC1 of L8 to produce, (c) Manually-derived lineaments.

Table 3
Bands of optical datasets, and their extracted number of lineaments in each spatial resolution category.

Pixel size	Spectral Range	Optical Datasets	band	Lineaments number
30m	VNIR	Landsat 8	1	706
			2	686
			3	768
			4	789
			5	753
		EO-1 ALI	1P	535
			1	578
			2	613
			3	599
			4	629
			4P	627
	SWIR	Landsat 8	6	784
			7	725
		ASTER	4	576
			5	539
			6	582
			7	423
			8	453
			9	459
		EO-1 ALI	5P	643
			5	751
			7	603
20m	VNIR	Sentinel 2A	5	1887
			6	1817
			7	1844
			8a	1770
	SWIR	Sentinel 2A	11	1574
			12	1446
15m	VNIR	Landsat 8	8	2951
		ASTER	1	2826
			2	2852
			3	2861
10m	VNIR	EO-1 ALI	pan	5795
		Sentinel 2A	2	7081
			3	7010
			4	6935
			8	6754

Table 4
The extracted number of lineaments for utilized DEMs, at different azimuths and altitudes.

Altitude (°)	Azimuth (°)	30 m pixel value			12.5 pixel value
		SRTM	NASA	ASTER	ALOS PALSAR
30	0	1052	1131	1231	9453
	45	913	1045	1189	9046
	90	868	1096	1054	8764
	135	955	1047	1053	9042
	180	1094	1186	1165	9303
	225	924	1034	1191	8886
	270	909	1037	1052	8946
	315	945	1048	1061	8960
45	0	1012	1148	1186	9438
	45	983	968	1075	8913
	90	905	971	932	8493
	135	915	1018	997	8933
	180	1047	1062	1210	9131
	225	910	1029	1084	8782
	270	868	934	1015	8887
	315	975	1062	1035	9043

established to be compared with the other composites. Pan sharpened 15m L8 RGB 752 composite, PC1 of L8, and ASTER VNIR bands were used collectively to visually interpret and manually delineate lineaments for the study area as shown in Fig. 2.

3. Results

Ample findings were obtained (e.g. The best VNIR and SWIR bands for each type of optical data, and the overall best data type for each resolution category) as shown in Tables 3 and 4, and Fig. 3**.** For single-band analysis of L8, the superiority of VNIR b8 is evident over all other bands by extracting 2951 lines and this undoubtedly is interpreted by its higher spatial resolution (15m) compared to the other bands (30m). For the other bands (1–7), b4 proved its efficiency by getting 789 lines compared to the others. However, PC1 of the seven pan-sharpened stacked bands, with the higher resolution b8 gives the maximum number of lines (3108) for L8. This is attributed to gathering the advantages of finer resolution and a higher amount of transformed data in the utilized PC1 (15m). Hence, data transformation and using the first principal component is recommended for lineament extraction from Landsat OLI data. For ASTER data, single VNIR band 3 gives 2861 lines compared to PC1 (15m) obtained 2756 lines and this could be interpreted by higher data variance in VNIR band 3. This could be explained by the data exuberance in VNIR bands, and this is confirmed by the previous studies (e.g. (El-Magd et al., 2015; Hung et al., 2005; Shebl et al., 2021)) which always recommend VNIR b3 of ASTER as one of the most efficient sources to extract lineaments. Concerning EO-1 ALI and by a number exceeding all the results of ASTER and L8, the panchromatic band (10m) of this sensor extracts 5795 lines manifesting the spatial resolution effect in this process. Sentinel 2 fulfilled the maximum ultimate number for all-optical sensors by its VNIR b2 (7081 lines).

DEMs are still efficient sources for comprehensive terrain, and morphometric analysis (Ashmawy et al., 2018) besides lineaments elicitation through hill shade analysis, and its supremacy over all the optical multispectral data, having the same resolution, is boosted in this study. In other words, the smallest number of extracted lines from DEMs exceeds the highest one extracted from multispectral data, provided that, both sources have the same pixel value Fig. 3a. Consequently, DEMs are strongly recommended over multispectral data in lineament extraction. Among SRTM, NASA, and ASTER DEMs, the latter evidenced its superiority over the formers by extracting 1231 lines compared to 1052 for SRTM DEM and 1148 for NASA DEM, as described in Table 4, at the same azimuth (0° or 180°). Which in turn, indicates the predominance of EW, NW-SE, NE-SW DEM extracted lineaments, coinciding with the structural setting of the study area (Zoheir et al., 2019a). We also considered the differences in timings of DEMs acquisition, which may result in any movements by selecting a case study of low geodynamics in the last 20 years compared to the coastal and northern part of the Red Sea (around the Gulf of Suez and the Gulf of Aqaba) (Abd El Nabi, 2012; Mohamed et al., 2019; Sawires et al., 2015). Moreover, we performed 16 lineament extraction processes for each DEMs over the main eight azimuths and by different angles, and ASTER DEM supremacy was confirmed over SRTM and NASA DEMs in all directions as shown in Table 4. ALOS PALSAR is the fourth DEM implemented for this study with its finer resolution of 12.5 m, outweighs all the data types and numbers in its ability to extract lineaments by giving the topmost lineaments number (9453) (Fig. 3a and b) at the 0° azimuths and 30° altitudes. This number obviously confirms the robustness of DEMs in lineament extraction especially if they are built from radar data. Thus, ALOS PALSAR DEM is strongly recommended for usage in geological applications. Besides that, this number introduced an odd issue to the well-established inversely proportional relationship between the pixel value and the extracted number of lineaments as it transcends the number of lines extracted from all 10 m optical data with its 12.5m resolution Fig. 3b. Over and above, it also surpasses sentinel 1 (VH and VV, 8229 and 9043 respectively, which also have a cell size of approximately 10m. The best results of lineament maps from different categories are displayed in Fig. 4 a-h. It is should be emphasized that these results are surely valid for orogenic belts and rugged terrains of arid environments. In these regions, abundant mineral deposits could be found and mostly controlled with the tectonic lineaments, thus the more

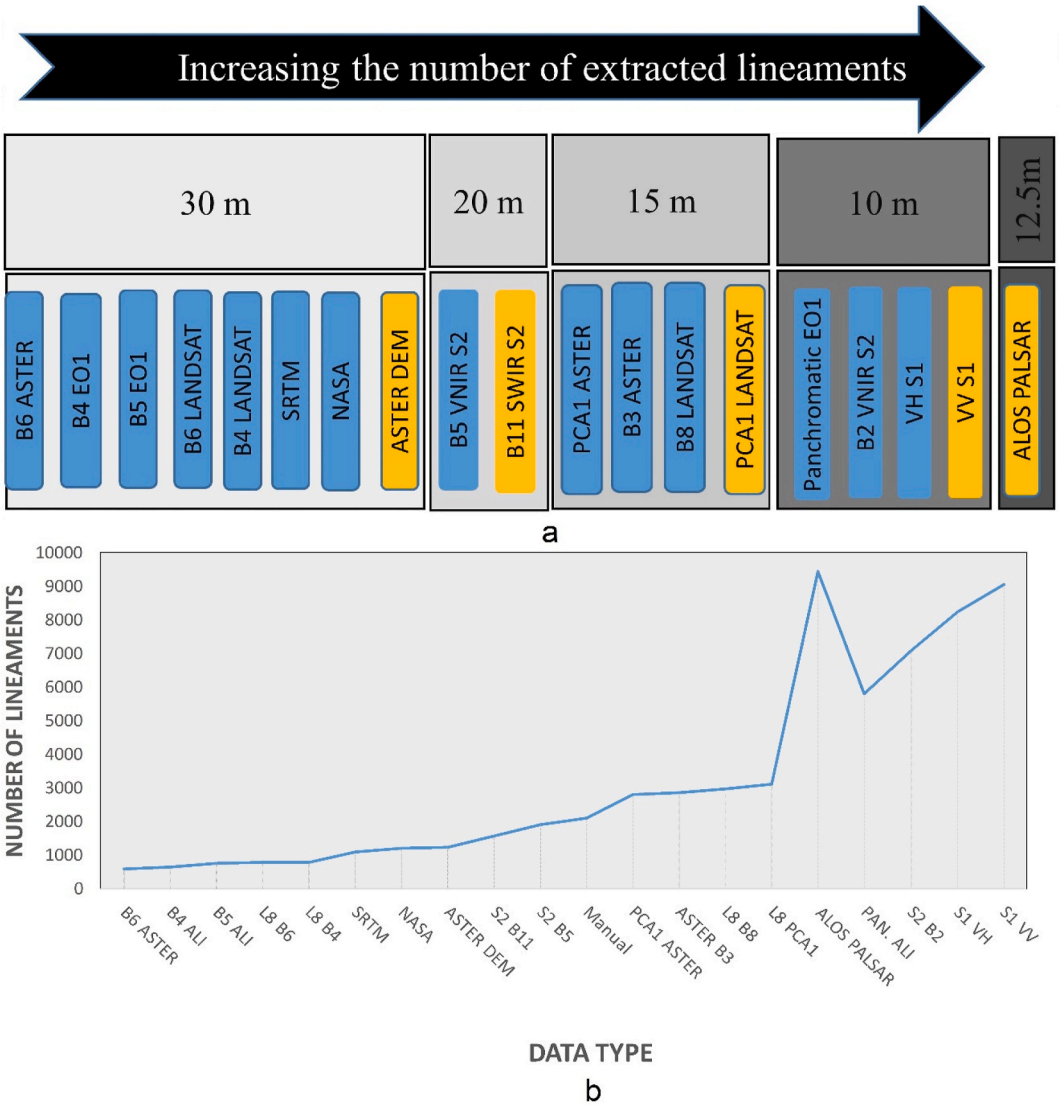

Fig. 3. (a) The best data types are ordered according to the ability of lineaments extracting, in each spatial resolution category (b) Ordering of the best data types, showing directly proportional relationship of extracted number of lineaments and pixel resolution except an odd behavior of ALOS PALSAR DEM reflecting its notability over all the used data at the study area.

efficient the data source implemented in extracting linear features the better fathoming of promising tectonic trends of several economic deposits. Other conditions (e.g. humid, vegetated, and densely populated regions) may affect the extracted number of lineaments. It should also be emphasized that the extracted number of lineaments considerably varies from one rock type to another depending on inherent lithological properties (e.g., claystone generally exhibits higher lineament density compared to limestones), tectonic setting, geomechanical situation, etc. Thus, the study measures the total number of lineaments extracted from various rock units within the same area, to ensure a wise evaluation (the registered numbers are extracted from 9 lithological units not only homogenous rock units.

3.1. Lineament lengths analysis

At 30 m spatial resolutions, the best data could be ordered in the next sequence started with the ablest in extracting lineaments as follows, ASTER DEM, NASA DEM, SRTM DEM, VNIR b4 L8, SWIR b6 L8, VNIR b4 EO1, and SWIR b6 ASTER (Fig. 3a). For all of these data, the highest percentage of lineaments numbers have lengths between 400 and 600 m and are arranged as follows 26.64%, 26.13%, 25.80%, 24.96%, 23.72%, 23.68%, and 22.16% respectively, as shown in Fig. 5 a–d. At 20 m pixel size, the highest percentage of lineaments numbers are of lengths ranging between 200 and 400 m and are registered for VNIR S2 b5 (Fig. 5 e) and SWIR S2 b11 as, 41.38% and 38.43%, respectively. At 15 m spatial resolution data (PC1 L8, panchromatic L8 b8, ASTER VNIR b3, and PC1 ASTER) the dominant line lengths are between 200 and 300 m, and by percentages of 24.38%, 22.83%, 23.83%, and 23.7% respectively (Fig. 5 f and g). At 12.5 m spatial resolution, ALOS PALSAR DEM followed the rule by giving prevailing line lengths as 100–200m and 200–300m, with a percentage of 31.31% and 23.23% respectively (Fig. 5 h). Decreasing the line lengths with lowering pixel size is still the controlling affair when 10 m pixel resolution data (Panchromatic EO1, VNIR sentinel 2 band 2, VH Sentinel 1, and VV sentinel 1) showed the predominant lineament lengths as 100–200 m by the following percentages 34.6%, 37.00%, 39.89%, and 41.19% respectively (Fig. 5 i–l).

3.2. Accuracy assessment

3.2.1. Density

Density and lineaments analyses seem to be inseparable, as the former estimates the concentration of the latter per unit area (Lachaine,

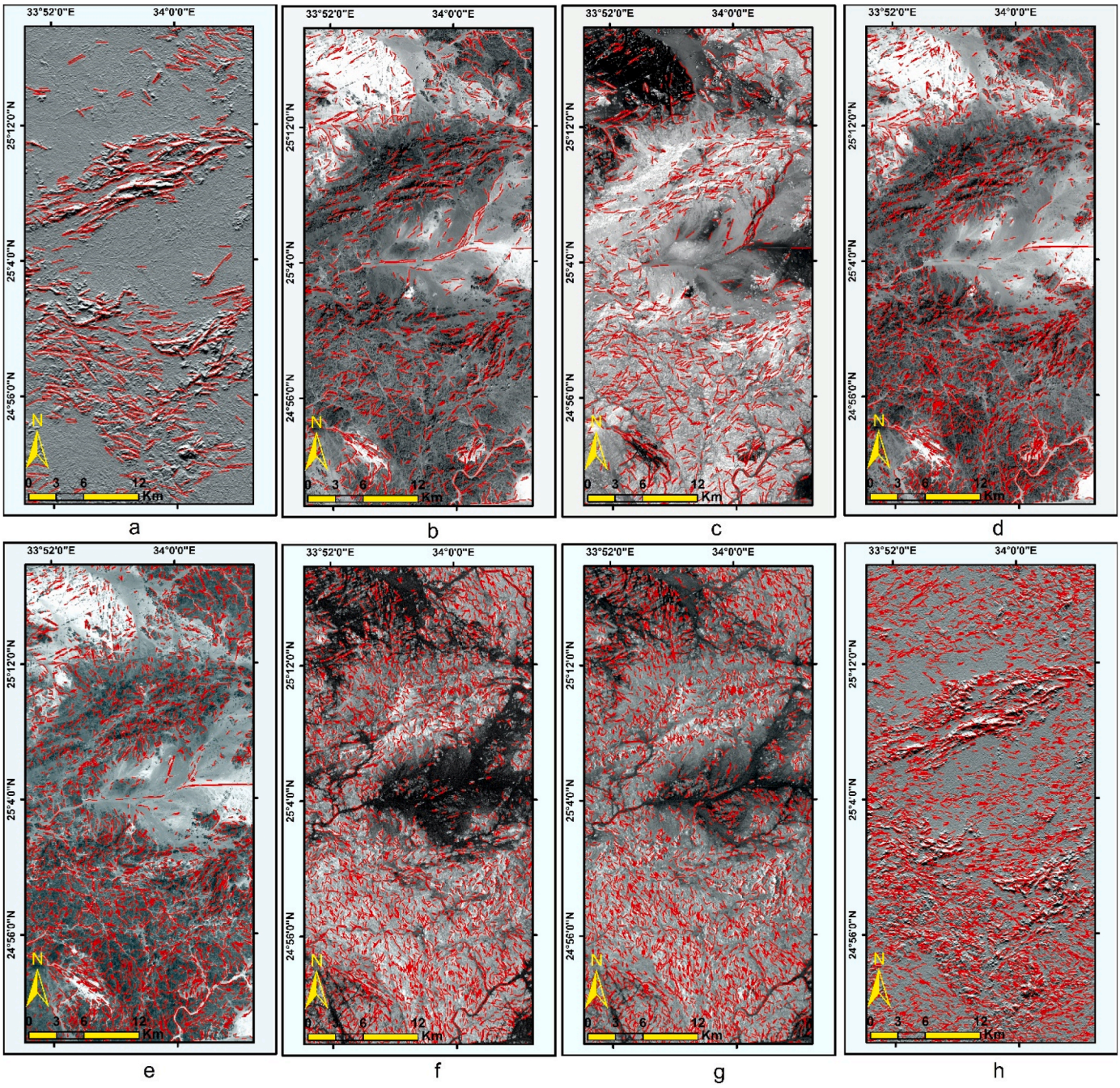

Fig. 4. Grey scale images of: (a) Shaded relief map of ASTER GDEM and, (b) ASTER b3, (c) PC1 of L8, (d) Panchromatic ALI, (e) S2 b2, (f) S1 VH, (g) S1 VV and, (h) Shaded relief map (0°–30°) of ALOS PALSAR DEM, overlaid by lineaments derived from each of them.

1999), thus, clearly displays their distribution. In the current study, the results are verified through the following steps.

1 Overlaying manually digitized confirmed faults over density maps gives reasonable fitting for all the data sources (Fig. 6 a).
2 Correlating density maps with two detailed (0.5 km scale) geological maps of Dungash and Samut areas (Zoheir et al., 2019b; Zoheir and Weihed, 2014). An outstanding matching is noticed, where the maps match well with higher to medium density regions proportional to the number of lines and their distribution on the geological maps as shown in Fig. 6 b–f.
3 Correlating the number of lines for higher density areas with visually interpreted lines to be able to answer the following question. Are those extracted lines (reflected as a high-density area) reasonably distributed, and reflect real linear features or not? To answer this question, we selected Gabal Mueilha area, which is composed mainly of post-orogenic alkali feldspar granite. So, ALI 752 RGB composite is prepared as it offers the best display for the linear features of Gabal Mueilha. After that, lines from different sources are dropped over Gabal Mueilha, and the best matching was noticed between the lines and real faults, fractures, and joints of Gabal Mueilha as shown in Fig. 6 g, h.

Generally, density analysis results have revealed that the southern part of the study area is denser than the northern part (Fig. 6 a). This could be interpreted by the presence of various lithologies with different elevations in the southern part (gabbros, granites, metavolcanics, serpentinites, and mélange) compared to the northern part of the study

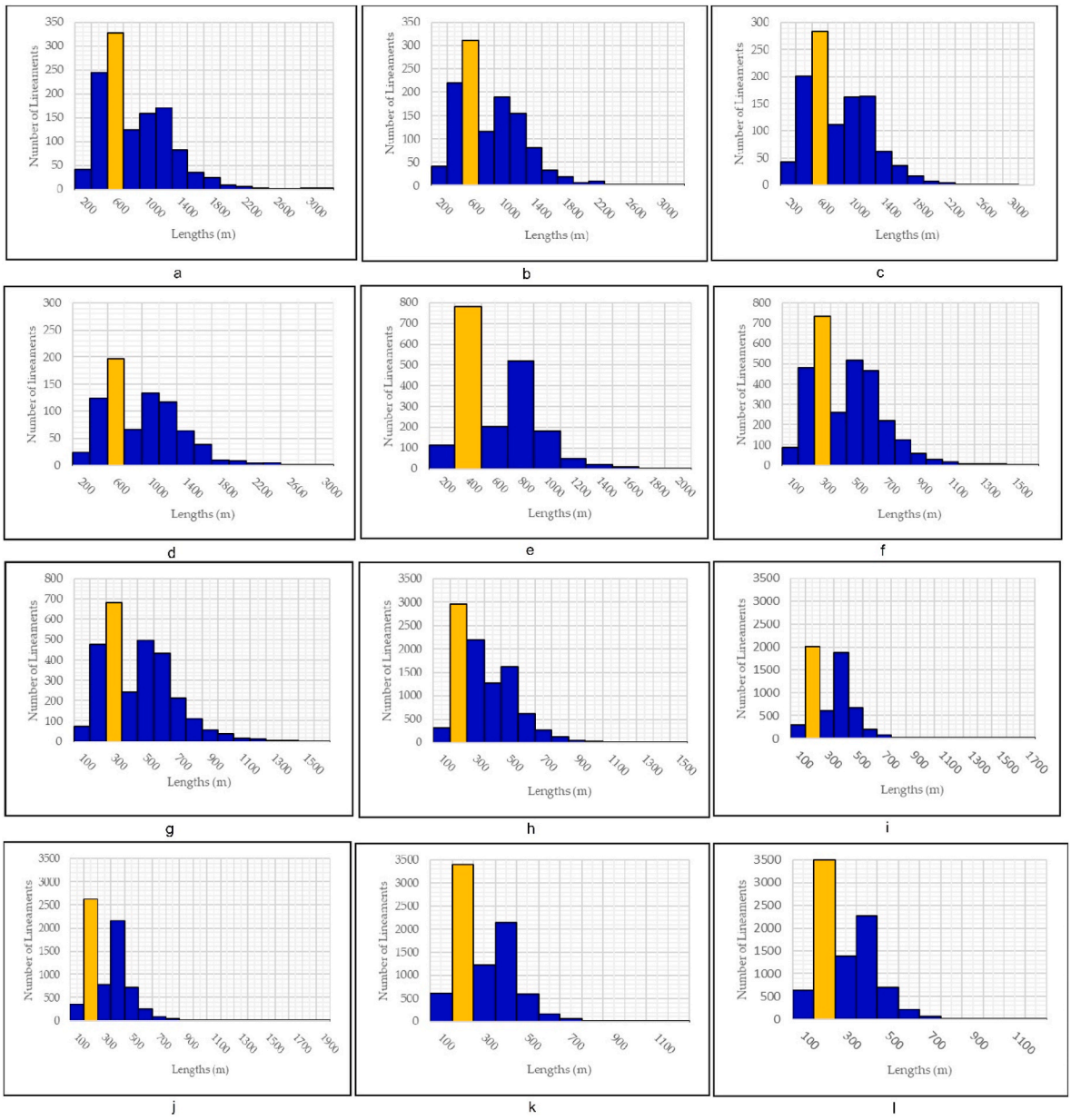

Fig. 5. Distribution histograms showing the lengths of lineaments from the different data types: (a) ASTER DEM, (b)NASA DEM, (c)SRTM DEM and, (d)VNIR b4 L8, manifesting 400–600 m lineament length as the dominant at 30m resolution. (e) 20m S2 b5, giving 200–400m as a dominant lineament length. At 15 m: (f) PC1 L8, and (g) ASTER VNIR b3, show the preference to 200–300m lineament lengths. (h) 12.5m ALOS PALSAR DEM manifest 100–200m lineament length as the dominant at this pixel size. (i) Panchromatic ALI, (j) VNIR sentinel 2 band 2, (k) VH Sentinel 1 and, (l) VV sentinel 1, giving 100–200 m as a dominant lineament length.

area, which is mainly occupied by extensively weathered granites and dykes. Consequently, more lithological boundaries, straightness of valleys, various slopes, and shades due to the variable elevations, as well as, the manifested structural features that are still preserved, are reflected as lineaments compared to that vanished due to extensive weathering in the northern part. However, finer resolution radar DEMs (ALOS PALSAR) and Sentinel 1 data can reasonably extract some of these foliations and dykes in the northern granitic bodies reflected as higher density areas, which again reflect the suitability of radar data in lineament extraction over various conditions. The central part of the study area is obviously divided into 2 main distinct zones: the northern central (higher density) and the southern central (lower density). The northern central high-density region is represented by Gabal Um Salatit and Gabal Um Salim areas.

They possess high elevations, different slopes, aspects, and hill shades which are directly reflected as lineaments. The best evidence for this interpretation is the manifestation of these areas in all the DEMs irrespective of their type or even their resolution and by a density value exceeding that derived from optical data. In contrast, and nearly for all the density maps, the flat area in the southern central part around the latitude of 25° 4" N, consists mainly of wadi deposits and mining work tailings appeared as lower density areas.

3.2.2. *Orientations and trend analysis*

This analysis easily identifies the predominant directions of lineaments by counting the frequent directions and exemplifying them via rose diagram petals. An accurate comparison between the result of this analysis (predominant bearings) with the prevailing lineaments trends of previous studies boost the study and is considered as a verification way for the study results (Hashim et al., 2013; Lachaine, 1999; Meshkani et al., 2013). Toward this target, the percentage of the total population (lineaments) are represented using petal radii in the angular spacing of

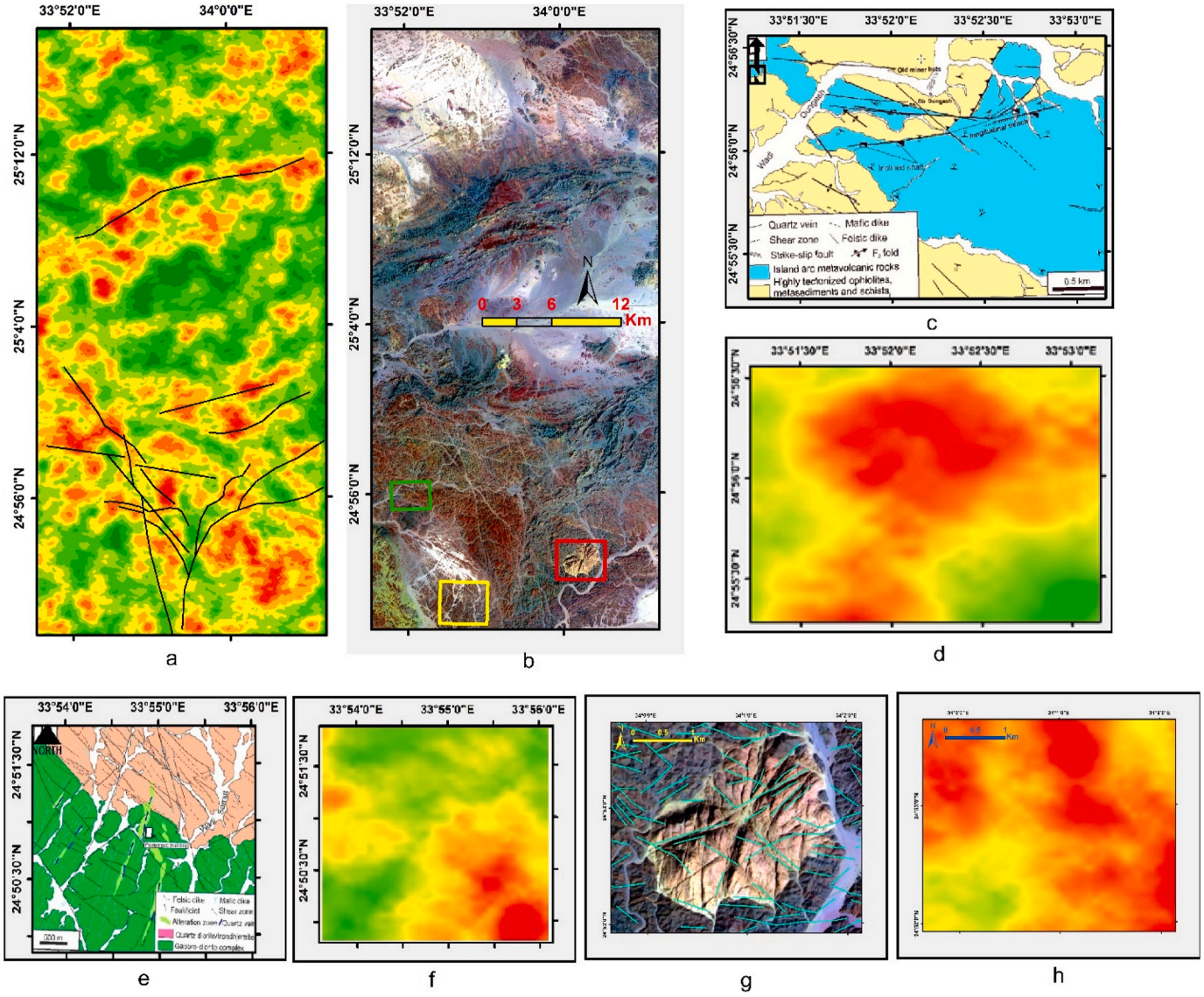

Fig. 6. (a) Density map of lineaments extracted from ALOS PALSAR DEM, overlain by manually digitized faults from the geological map, (b) RGB 752 L8 composite as a location map for the three selected test areas (green box is Dungash, the yellow box is Samut and red box is Mueilha), (c) Dungash geologic map (Zoheir and Weihed, 2014), and (d) Its ALOS PALSAR DEM density map, (e) Samut geologic map (Zoheir et al., 2019b), and (f) Its ALOS PALSAR DEM density map, (g) Pan-sharpened 10m RGB 752 ALI image of Gabal Mueilha superimposed by automatically extracted lineaments from ALOS PALSAR DEM, and (h) its density map. (For interpretation of the references to color in this figure legend, the reader is referred to the Web version of this article.)

15° half style rose diagrams with numbered half-circles indicating the frequencies. The results from optical L8, ASTER, ALI, and S2 b5 indicate that the predominant trends are NE-SW and WNW-ESE as shown in Fig. 7 a–c. However, b2 of S2, with its higher number of lineaments and shorter lengths gives the predominance to NNE-SSW direction with preserving NE-SW and WNW-ESE trend as the second common trend, (Fig. 7 d). Consequently, it is noticed that when the lineaments get shorter (by increasing spatial resolution), the vertical trending becomes controlling with preserving the common NE-SW and WNW-ESE. This case is confirmed by S1 VH and VV polarizations that give the preference to NNE-SSW, NNW-SSE, and NW-SE rather than NE-SW and WNW-ESE (Fig. 7 e–f). For DEMs, the highest numbers of lineaments are obtained by azimuths (0° and 180°) and by performing trend analysis for this product, it is reasonably noticed the absence of sub-vertical trend but manifesting the other 3 main trends as shown in Fig. 7 g.

Overall and from the whole trend analysis, it is deduced that preferred lineaments trends could be grouped into 4 main categories as follow, (1) Sub-vertical trends (NNE-SSW to NNW-SSE), (2) Sub-horizontal trends (ENE-WSW to WNW-ESE), (3) NE-SW and, (4) NW-SE, as shown in Fig. 7. These results are embedded into a profound and careful geologic evaluation with the detailed previous studies. The extracted trends perfectly coincide with recently published results concerning the structural setting of the study area. This study grouped the deformation phases and their relevant structures into 3 main phases D1, D2, and D3 (Zoheir et al., 2019a). D1 is NNW–SSE shortening, which is responsible for NE- SW trending lines, D2 is NNE-SSW Shortening results in NW–SE trends. Moreover, D1 and D2 collectively participated in the generation of sub-horizontal trends (ENE-WSW to WNW-ESE). Whereas, lines possessing sub-vertical trends (NNE-SSW to NNW-SSE) resulted from the D3 phase named as E–W Oblique Convergence.

4. Discussion

Due to the great importance of lineaments in several applications, convenient and serviceable automated extraction methods, several researchers studied lineament extraction from optical and radar satellite

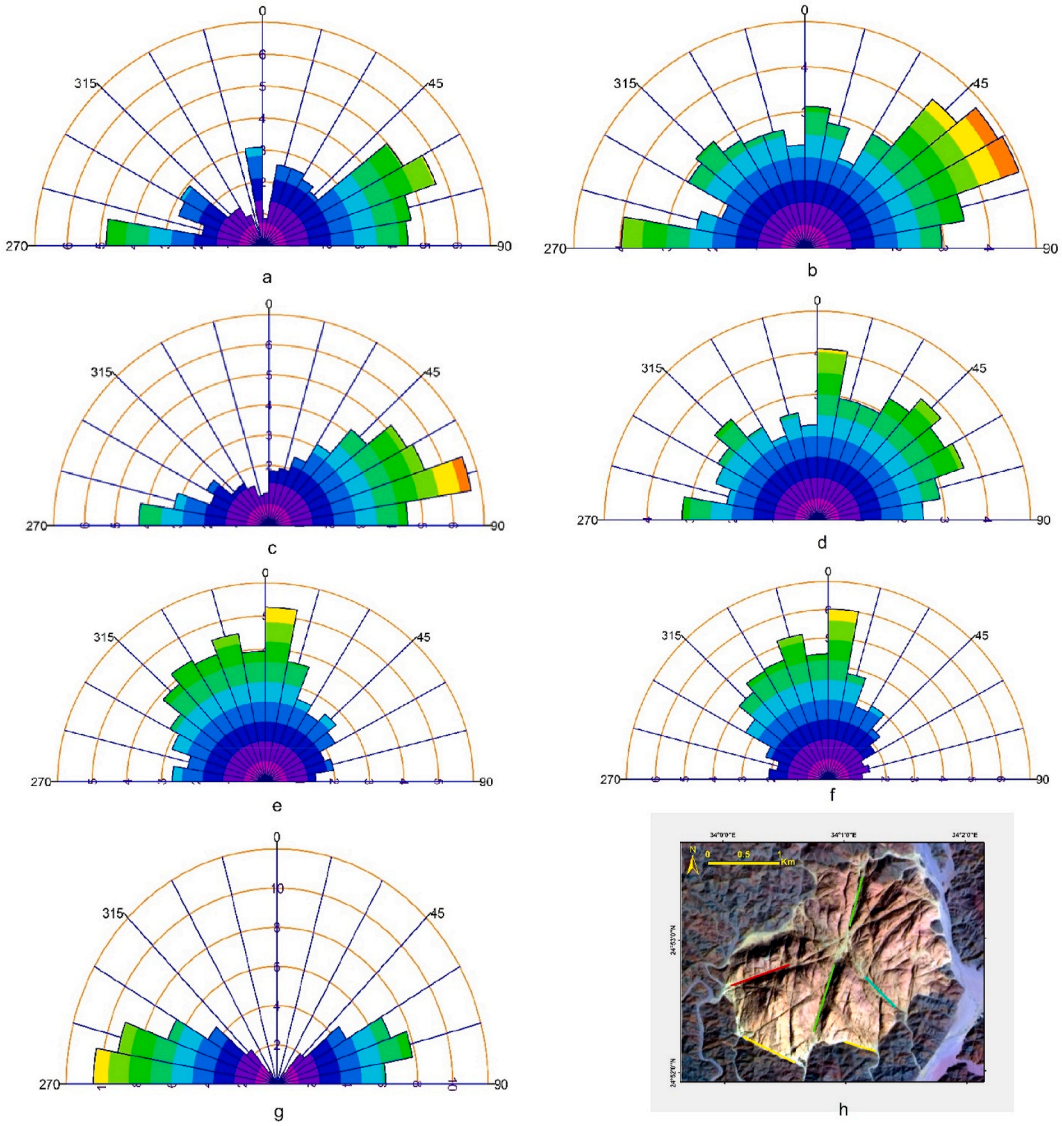

Fig. 7. Rose diagrams showing the orientations of lineaments extracted from: (a) ASTER b6; (b) S2 b5; (c) ASTER b3; (d) S2 b2; (e) S1 VH; (f) S1 VV and; (g) ALOS PALSAR DEMs, at azimuth (0°) and altitude (30°). (h) manifestation of the four common trends over Gabal Mueilha: Sub-vertical trends (NNE-SSW to NNW-SSE) is represented by green line; Sub-horizontal trends (ENE-WSW to WNW-ESE) is highlighted by yellow lines; NE-SW trend is represented by red color and cyan color for denoting NW-SE orientation. Moreover, and in a sinistral sense of displacement, the yellow lines are shifted in a way manifesting the existence of NNE-SSW fault (green line). (For interpretation of the references to color in this figure legend, the reader is referred to the Web version of this article.)

data (Bruning et al., 2011; Koçal, 2004; Mostafa and Bishta, 2005), and DEMs (Abdullah et al., 2010; Al-Obeidat et al., 2016). However, the implemented studies in comparing lineaments from various data sources are still countable. Authors of (Hung et al., 2005)compared the extracted lineaments from Landsat ETM and ASTER images and stated that the VNIR band 3 of ASTER and the fused band 4 of the Landsat ETM gave the best results. Furthermore, the authors (Op. cit.) stated that the accuracy of extracted lineaments relies mainly on the spatial resolution of the imagery, a higher resolution imagery results in a higher quality of lineament map. This is not always the case in remote sensing studies and this concept needs to be better outlined and limited in remote sensing studies by adding the next sentence "for the same data type". For example, in this study, ALOS PALSAR DEM (12.5m) provided a better lineament extraction result than the finer S1 & S2 (10m bands). Furthermore, in this study, VNIR ASTER imagery considerably shows higher accuracy in lineament extraction than even its PCs, which is congruous with earlier observations of (El-Magd et al., 2015; Hung et al., 2005; Shebl et al., 2021). Authors of (Adiri et al., 2017) compared ASTER, Landsat 8, and Sentinel 1 images in their efficiency in lineament extraction and clarified great efficiency in automatic lineaments extraction of the latter, compared to the formers, which is confirmed by observations of this study. They (Adiri et al., 2017) accentuated the role of Sentinel 1 VH polarization, contrary to this study, which shows the better performance of VV than VH polarization. One of the recent studies (Javhar et al., 2019) compared Sentinel 2, Landsat 8, and Sentinel 1 images and in a harmony with the current results, emphasized the great fulfillment of radar data over optical data in lineament extraction.

DEM superiority over optical data is interpreted by its independence from sensor characteristics (Sahoo et al., 2018), and radar superiority is referred to the absence of weather conditions effect (Adiri et al., 2017). S1 (C-band) is less efficient when compared to ALOS PALSAR (L-band) data especially in this arid environment where L-band radar waves capability of penetration become higher for thin sedimentary covers revealing more subsurface information. The spatial resolution effect of several data types needs to be considered and data of the same pixel size should be compared together. In this study, the comparison incorporated pixel size to be wise enough to compare the capability of data as it is unfair, for example, to compare ASTER and Landsat 8 (15m or 30m) to

sentinel VV and VH (10m). It is worth mentioning that manual lineament extraction or at least visual check of the automatically extracted lineaments is still indispensable whatever the implemented data source or the applied technique. Of course, automatic lineament extraction could save time, effort, avoid estimation errors, be independent of image qualities or user experiences, increases objectivity (based on a computer algorithm) rather than subjectivity (Ramli et al., 2010) accompanied with manual methods. However, manual methods could easily set apart tectonic and anthropogenic linear features (Javhar et al., 2019) and assign full chronological sequences between the derived lineaments (e.g., detection of a relatively older lineament pattern overlain by a younger pattern) which is too difficult in automatic technique. The latter is a valuable additional tool for the structural analysis, however, it has to be combined into a thorough geologic evaluation.

5. Conclusions

In this study, Landsat OLI, ASTER, EO 1 ALI, Sentinel 2A, ALOS PALSAR, SRTM, NASA, ASTER V3 DEMs, and Sentinel 1 were evaluated for their competence in lineament extraction. Their results are ordered based on the pixel size value aiming to recommend this scheme to the geological scientific community. Our main findings are.

- At 30 m spatial resolution, the preferred optical data types recommended for usage, for each data type, are ASTER (b6 SWIR), ALI (b5 SWIR, b4 VNIR), and L8 (b6 SWIR, b4 VNIR) as the best data source for this pixel size. At the same resolution, DEMs are arranged according to their efficiency in extracting lineaments as SRTM, NASA, and ASTER v3 as the best.
- At 20 m, S2 b5 VNIR exceeds S2 b11 SWIR.
- At 15 m pixel value, in increasing order, the best data are PC1 ASTER, ASTER b3, L8 b8, and L8 PC1 as the best source for extracting lineaments.
- At 12.5 m pixel value, ALOS PALSAR gives an outstanding result that exceeds all the implemented data types whatever their pixel size value.
- At 10 m cell size, radar VH & VV polarizations overcome optical data of panchromatic band of EO1 ALI and S2 b2.

The novelty in this study could be concluded in comparing nine different data types, categorized according to their spatial resolution, in lineaments extraction. The study pointed out that DEMs and radar data exceeds optical data sources in their capability of lineament extraction. DEM preponderance may be due to independence from sensor characteristics. Radar superiority could be explained by the sensitivity of the radar data to geomorphology without affecting by weather conditions, whereas the optical data are influenced by the shading areas as well as, by the occupation of the soil. Also, radar data could extract lineaments from completely weathered or approximately vanished rock units. Consequently, combining DEM with Radar data (e.g., PALSAR DEM) transcend sentinel 1 (that is always recommended by researchers) by a rate that could exceed the known relationship between pixel size and the number of extracted lineaments. Finally, the study recommended the best data types (depending mainly on the extracted number of lineaments and pixel size), commonly used in geological applications over a wide range of pixel values (10, 12.5.15, 20, 30m) to meet the requirements of the majority of geological studies and to help the users give the most potential results depending on implementing the most efficient data type.

Funding

This research received no external funding. This research is supported by University of Debrecen. Ali Shebl is funded by Stipendium Hungaricum scholarship under the joint executive program between Hungary and Egypt.

Declaration of competing interest

The authors declare that they have no known competing financial interests or personal relationships that could have appeared to influence the work reported in this paper.

The authors declare no conflict of interest.

Acknowledgments

The authors are thankful to U.S. Geological Survey, Alaska satellite facility and European Space Agency (ESA), for providing the data. Thanks to Prof. Mahmoud Ashmawy, Prof. Mohamed Abd El-wahed and Prof. Samir Kamh, for their kind support. The authors also greatly appreciate the referee's valuable and profound comments.

References

Abd El Nabi, S.H., 2012. Curie point depth beneath the Barramiya–Red Sea coast area estimated from spectral analysis of aeromagnetic data. J. Asian Earth Sci. 43, 254–266. https://doi.org/10.1016/J.JSEAES.2011.09.015.

Abd El-Wahed, M.A., Zoheir, B., Pour, A.B., Kamh, S., 2021. Shear-related gold ores in the wadi hodein shear belt, south eastern desert of Egypt: analysis of remote sensing, field and structural data. Minerals 11, 474. https://doi.org/10.3390/min11050474.

Abdullah, A., Akhir, J.M., Abdullah, I., 2010. Automatic mapping of lineaments using shaded relief images derived from digital elevation model (DEMs) in the Maran–Sungi Lembing area, Malaysia. Electron. J. Geotech. Eng. 15, 949–958.

Adhab, S.S., Hassan, M.A., 2014. Lineament automatic extraction analysis for Galal Badra river basin using Landsat 8 satellite image. Iraqi J. Phys. 12, 44–55.

Adiri, Z., El Harti, A., Jellouli, A., Lhissou, R., Maacha, L., Azmi, M., Zouhair, M., Bachaoui, E.M., 2017. Comparison of Landsat-8, ASTER and Sentinel 1 satellite remote sensing data in automatic lineaments extraction: a case study of Sidi Flah-Bouskour inlier, Moroccan Anti Atlas. Adv. Sp. Res. 60, 2355–2367.

Akinluyi, F.O., Olorunfemi, M.O., Bayowa, O.G., 2018. Investigation of the influence of lineaments, lineament intersections and geology on groundwater yield in the basement complex terrain of Ondo State, Southwestern Nigeria. Appl. water Sci. 8, 49.

Al-Obeidat, F., Feltrin, L., Marir, F., 2016. Cloud-based lineament extraction of topographic lineaments from NASA shuttle radar topography mission data. Procedia Comput. Sci. 83, 1250–1255.

Alizadeh, M., Ngah, I., Hashim, M., Pradhan, B., Pour, A.B., 2018. A hybrid analytic network process and artificial neural network (ANP-ANN) model for urban earthquake vulnerability assessment. Rem. Sens. 10, 975.

Ashmawy, M.H., Abd El-Wahed, M.A., Kamh, S.Z., Shebl, A., 2018. Scientific Journal of Basic and Applied Sciences Comparative study of the drainage basin morphometry extracted from topographic maps and SRTM DEMs: an example from Ghadir watershed, Eastern Desert, Egypt. Sci JBAS 39, 52–64.

Ashournejad, Q., Hosseini, A., Pradhan, B., Hosseini, S.J., 2019. Hazard zoning for spatial planning using GIS-based landslide susceptibility assessment: a new hybrid integrated data-driven and knowledge-based model. Arab. J. Geosci. 12, 126.

Bhuiyan, C., 2015. Hydrological characterisation of geological lineaments: a case study from the Aravalli terrain, India. Hydrogeol. J. 23, 673–686.

Bruning, J.N., Gierke, J.S., Maclean, A.L., 2011. An approach to lineament analysis for groundwater exploration in Nicaragua. Photogramm. Eng. Remote Sens. 77, 509–519.

Corgne, S., Magagi, R., Yergeau, M., Sylla, D., 2010. An integrated approach to hydro-geological lineament mapping of a semi-arid region of West Africa using Radarsat-1 and GIS. Remote Sens. Environ. 114, 1863–1875.

Dasho, O.A., Ariyibi, E.A., Akinluyi, F.O., Awoyemi, M.O., Adebayo, A.S., 2017. Application of satellite remote sensing to groundwater potential modeling in Ejigbo area, Southwestern Nigeria. Model. Earth Syst. Environ. 3, 615–633.

El-Magd, I.A., Mohy, H., Basta, F., 2015. Application of remote sensing for gold exploration in the Fawakhir area, Central Eastern Desert of Egypt. Arab. J. Geosci. 8, 3523–3536. https://doi.org/10.1007/s12517-014-1429-4.

Engdahl, M.E., Hyyppa, J.M., 2003. Land-cover classification using multitemporal ERS-1/2 InSAR data. IEEE Trans. Geosci. Remote Sens. 41, 1620–1628.

Hashim, M., Ahmad, S., Johari, M.A.M., Pour, A.B., 2013. Automatic lineament extraction in a heavily vegetated region using Landsat Enhanced Thematic Mapper (ETM+) imagery. Adv. Sp. Res. 51, 874–890.

Hong, S.H., Wdowinski, S., 2014. Multitemporal multitrack monitoring of wetland water levels in the florida everglades using alos palsar data with interferometric processing. IEEE Geosci. Remote Sens. Lett. 11, 1355–1359. https://doi.org/10.1109/LGRS.2013.2293492.

Hung, L.Q., Batelaan, O., De Smedt, F., 2005. Lineament extraction and analysis, comparison of LANDSAT ETM and ASTER imagery. Case study: Suoimuoi tropical karst catchment, Vietnam. In: Remote Sensing for Environmental Monitoring, GIS Applications, and Geology V. International Society for Optics and Photonics, p. 59830T.

Ibrahim, U., Mutua, F., 2014. Lineament extraction using landsat 8 (OLI) in Gedo, Somalia. Int. J. Sci. Res. 3, 291–296.

Javhar, A., Chen, X., Bao, A., Jamshed, A., Yunus, M., Jovid, A., Latipa, T., 2019. Comparison of multi-resolution optical Landsat-8, Sentinel-2 and radar Sentinel-1

data for automatic lineament extraction: a case study of Alichur area, SE Pamir. Rem. Sens. 11, 778.
Koçal, A., 2004. A Methodology for Detection and Evaluation of Lineaments from Satellite Imagery.
Koike, K., Ichikawa, Y., 2006. Spatial correlation structures of fracture systems for deriving a scaling law and modeling fracture distributions. Comput. Geosci. 32, 1079–1095.
Lachaine, G., 1999. Structures géologiques et linéaments, Beauce (Québec): apport de la télédétection. Université de Sherbrooke.
Magaia, L.A., Goto, T., Masoud, A.A., Koike, K., 2018. Identifying groundwater potential in crystalline basement rocks using remote sensing and electromagnetic sounding techniques in central western Mozambique. Nat. Resour. Res. 27, 275–298.
Manuel, R., Brito, M.D.G., Chichorro, M., Rosa, C., 2017. Remote sensing for mineral exploration in central Portugal. Minerals 7, 184.
Marghany, M., Hashim, M., 2010. Lineament mapping using multispectral remote sensing satellite data. Int. J. Phys. Sci. 5, 1501–1507.
Masoud, A., Koike, K., 2006. Tectonic architecture through Landsat-7 ETM+/SRTM DEM-derived lineaments and relationship to the hydrogeologic setting in Siwa region, NW Egypt. J. Afr. Earth Sci. 45, 467–477.
Masoud, A.A., Koike, K., 2011. Auto-detection and integration of tectonically significant lineaments from SRTM DEM and remotely-sensed geophysical data. ISPRS J. Photogramm. Remote Sens. 66, 818–832.
Meshkani, S.A., Mehrabi, B., Yaghubpur, A., Sadeghi, M., 2013. Recognition of the regional lineaments of Iran: using geospatial data and their implications for exploration of metallic ore deposits. Ore Geol. Rev. 55, 48–63.
Mohamed, A.E.-E.A., El-Hadidy, M., Deif, A., Elenean, K.A., 2019. Seismic hazard studies in Egypt. https://doi.org/10.1016/j.nrjag.2012.12.008 1. https://doi.org/10.1016/J.NRJAG.2012.12.008, 119-140.
Mostafa, M.E., Bishta, A.Z., 2005. Significance of lineament patterns in rock unit classification and designation: a pilot study on the Gharib-Dara area, northern Eastern Desert, Egypt. Int. J. Rem. Sens. 26, 1463–1475.
Muhammad, M.M., Awdal, A.H., 2012. Automatic mapping of lineaments using shaded relief images derived from digital elevation model (DEM) in Erbil-Kurdistan, northeast Iraq. Adv. Nat. Appl. Sci. 6, 138–147.
Nath, B., Niu, Z., Acharjee, S., 2017. Pre-Earthquake Anomaly Detection and Assessment through Lineament Changes Observation Using Multi-Temporal Landsat 8-OLI Imageries: Case of Gorkha and Imphal. Multi-Purposeful Appl. Geospatial Data.
Nath, B., Niu, Z., Mitra, A.K., 2019. Observation of short-term variations in the clay minerals ratio after the 2015 Chile great earthquake $$(8.3 M_ {\mathrm {w}}) $$ using Landsat 8 OLI data. J. Earth Syst. Sci. 128, 117.
Pirasteh, S., Pradhan, B., Safari, H.O., Ramli, M.F., 2013. Coupling of DEM and remote-sensing-based approaches for semi-automated detection of regional geostructural features in Zagros mountain, Iran. Arab. J. Geosci. 6, 91–99.
Pour, A.B., Hashim, M., 2015a. Structural mapping using PALSAR data in the central gold belt, Peninsular Malaysia. Ore Geol. Rev. 64, 13–22.
Pour, A.B., Hashim, M., 2015b. Integrating PALSAR and ASTER data for mineral deposits exploration in tropical environments: a case study from Central Belt, Peninsular Malaysia. Int. J. Image Data Fusion 6, 170–188.
Pour, A.B., Hashim, M., 2014. Structural geology mapping using PALSAR data in the Bau gold mining district, Sarawak, Malaysia. Adv. Sp. Res. 54, 644–654.
Pour, A.B., Hashim, M., Makoundi, C., Zaw, K., 2016. Structural mapping of the Bentong-Raub Suture zone using PALSAR remote sensing data, Peninsular Malaysia: implications for Sediment-hosted/orogenic gold mineral systems exploration. Resour. Geol. 66, 368–385.
Qari, M.H.T., 2011. Lineament extraction from multi-resolution satellite imagery: a pilot study on wadi Bani Malik, Jeddah, Kingdom of Saudi Arabia. Arab. J. Geosci. 4, 1363–1371.
Rahnama, M., Gloaguen, R., 2014. TecLines: a MATLAB-based toolbox for tectonic lineament analysis from satellite images and DEMs, part 1: line segment detection and extraction. Rem. Sens. 6, 5938–5958.
Ramli, M.F., Yusof, N., Yusoff, M.K., Juahir, H., Shafri, H.Z.M., 2010. Lineament mapping and its application in landslide hazard assessment: a review. Bull. Eng. Geol. Environ. 692, 215–233. https://doi.org/10.1007/S10064-009-0255-5, 2009, 69.
Richards, J.A., others, 2009. Remote Sensing with Imaging Radar. Springer.
Saepuloh, A., Haeruddin, H., Heriawan, M.N., Kubo, T., Koike, K., Malik, D., 2018. Application of lineament density extracted from dual orbit of synthetic aperture radar (SAR) images to detecting fluids paths in the Wayang Windu geothermal field (West Java, Indonesia). Geothermics 72, 145–155.
Sahoo, S., Das, P., Kar, A., Dhar, A., 2018. A forensic look into the lineament, vegetation, groundwater linkage: study of Ranchi District, Jharkhand (India). Remote Sens. Appl. Soc. Environ. 10, 138–152.
Sawires, R., Peláez, J.A., Fat-Helbary, R.E., Ibrahim, H.A., 2015. A review of seismic hazard assessment studies and hazard description in the building codes for Egypt. Acta Geod. Geophys. 2015 512, 151–180. https://doi.org/10.1007/S40328-015-0117-5, 51.
Shebl, A., Abdellatif, M., Elkhateeb, S.O., Csámer, Á., 2021. Multisource data analysis for gold potentiality mapping of Atalla area and its environs, central Eastern Desert, Egypt. Miner. 2021 (11), 641. https://doi.org/10.3390/MIN11060641, 641 11.
Singh, P.P., Garg, R.D., 2013. Study of spectral reflectance characteristics of asphalt road surface using geomatics techniques. In: 2013 International Conference on Advances in Computing, Communications and Informatics (ICACCI). IEEE, pp. 516–520.
Sukumar, M., Venkatesan, N., Nelson Kennedy Babu, C., 2014. A review of various lineament detection techniques for high resolution satellite images. Int. J. Adv. Res. Comput. Sci. Software Eng. 4, 72–78.
Takorabt, M., Toubal, A.C., Haddoum, H., Zerrouk, S., 2018. Determining the role of lineaments in underground hydrodynamics using Landsat 7 ETM+ data, case of the Chott El Gharbi Basin (western Algeria). Arab. J. Geosci. 11, 76.
Tripathi, N.K., Gokhale, K., Siddiqui, M.U., 2000. Directional morphological image transforms for lineament extraction from remotely sensed images. Int. J. Rem. Sens. 21, 3281–3292.
Zoheir, B., El-Wahed, M.A., Pour, A.B., Abdelnasser, A., 2019a. Orogenic gold in transpression and transtension zones: field and remote sensing studies of the barramiya–mueilha sector, Egypt. Rem. Sens. 11, 2122.
Zoheir, B., Steele-MacInnis, M., Garbe-Schönberg, D., 2019b. Orogenic gold formation in an evolving, decompressing hydrothermal system: genesis of the Samut gold deposit, Eastern Desert, Egypt. Ore Geol. Rev. 105, 236–257.
Zoheir, B., Weihed, P., 2014. Greenstone-hosted lode-gold mineralization at Dungash mine, Eastern Desert, Egypt. J. Afr. Earth Sci. 99, 165–187.